47th AIAA Aerospace Sciences Meeting Including The New Horizons Forum and Aerospace Exposition
5 - 8 January 2009, Orlando, Florida

AIAA 2009-322

An Aerodynamic Study of Bicycle Wheel Performance using CFD

Matthew N. Godo[1]
JMSI dba Intelligent Light, RutherFord, NJ, 07070

David Corson[2]
ACUSIM Software, Inc., Clifton Park, NY 12065

and

Steve M. Legensky[3]
JMSI dba Intelligent Light, RutherFord, NJ, 07070

A methodology is presented to apply CFD to study air flow around a rotating bicycle wheel in contact with the ground. The bicycle wheel studied here is an accurate geometrical representation of a commercial racing wheel (Zipp 404). Reynolds-Averaged Navier Stokes (RANS) and Delayed Detached Eddy Simulation (DDES) results are computed at a range of speeds and yaw angles commonly encountered by cyclists. Drag and side (or lift) forces are resolved and compare favorably to experimental results obtained from wind tunnel tests. Vertical forces acting on a rotating bicycle wheel are presented for the first time. A unique transition from downward to upward acting force is observed as the yaw angle is increased. Flow structures are identified and compared for different yaw angles. It is expected that a more complete comprehension of these results will lead to improvements in the performance and handling characteristics of bicycle racing wheels used by professional cyclists and triathletes.

Nomenclature

C_D = drag coefficient (= $F_D/0.5\rho\ V^2 \cdot S$)
C_S = side force coefficient (= $F_S/0.5\rho\ V^2 \cdot S$)
C_V = vertical force coefficient (= $F_V/0.5\rho\ V^2 \cdot S$)
D = nominal bicycle wheel diameter
F_D = axial drag force
F_S = side (or lift force)
F_V = vertical force
f = frequency
p = pressure
S = reference area, $\pi D^2/4$
St = Strouhal No. (= $f \cdot D/V$)
t* = dimensionless time (= $t \cdot V/D$)
u = velocity vector
V = bicycle speed

β = yaw angle
μ = viscosity
ρ = density

[1] FieldView Product Manager, Intelligent Light 301 Rt 17N, Rutherford NJ, Member AIAA.
[2] Senior Analyst, 634 Plank Road, Ste 205, Clifton Park, NY
[3] General Manager, Intelligent Light 301 Rt 17N, Rutherford NJ, Senior Member AIAA.

I. Introduction

The margin of victory separating the top three overall finishers of the Tour de France in 2007 was 31 seconds after nearly 90 hours of racing. In the last individual time trial discipline of this event, the top ten riders were separated by less than 3 minutes for a ride lasting slightly more than 1 hour. A seemingly small gain of 1%, or approximately 40 seconds, meant the difference between 3rd place and 8th place. Increasingly, manufacturers of racing bicycles and bicycle components have turned to wind tunnel testing to optimize component design[1] and individual rider position as shown in Figure 1. Owing to the wide variation in commercially available components, it is clear that design innovation is a vital part of this industry.

Figure 1. Optimization of riding position for a Triathlete in a low speed wind tunnel.

It is commonly recognized that main contributors to overall drag are the rider, the frame including fork and aerobars, and the wheels. Comprehensive reviews by Burke[2] and Lukes et.al.[3] cite many efforts to identify the most relevant contributions to overall performance improvements in bicycle racing. Greenwell et.al.[4] have concluded that the drag contribution from the wheels is on the order of 10% to 15% of the total drag, and that with improvements in wheel design, an overall reduction in drag on the order of 2% to 3% is possible. The wind tunnel results of Zdravkovich[5] demonstrated that the addition of simple splitter plates to extend the rim depth of standard wheels was seen to reduce drag by 5%. In the mid 1980's, commercial bicycle racing wheel manufacturers started to build wheels with increasingly deeper rims having toroidal cross sections[6,7]. The experimental studies published by Tew and Sayers[8] showed that the newer aerodynamic wheels were able to reduce drag by up to 50% when compared to conventional wheels. Although many wind tunnel tests have now been performed on bicycle wheels, it has been difficult to make direct comparisons owing to variations in wind tunnel configurations and the testing apparatus used to support and rotate the bicycle wheels studied. In the works published by Kyle and Burke[9,10,11] it was observed that a very significant reduction in drag was measured for rotating wheels when compared to stationary ones. Although the experimental work of Fackrell and Harvey[12,13,14] was applied to study the aerodynamic forces on much wider automobile tires, it is worth noting that they also observed a reduction in drag and side forces when comparing rotating and stationary wheels.

To date, far less work has been done to apply CFD to study the flow around a rolling wheel in contact with the ground. Wray[15] used RANS with standard k-ε and RNG k-ε turbulence models to explore the effect of increasing yaw angle for flow around a rotating car tire. He observed that the yaw angle was seen to have a strong association with the degree of flow separation occurring on the suction side of the wheel. A shortcoming of this study was the lack of experimental data available for comparison and the authors note this as a direction for future work. McManus et.al.[16] used an unsteady Reynolds Averaged Navier Stokes (URANS) approach to validate CFD against the experimental results of Fackrell and Harvey for an isolated rotating car tire in contact with the ground. The one-equation Spalart-Allmaras[17] (S-A) model and a two equation realizable k-ε turbulence model[18] (RKE) were used. The time averaged results from this study showed good qualitative and quantitative agreement with experimental data. The authors suggest that differences between their predictions on the rotating wheel and the wind tunnel results for surface pressures at the line of contact were due to errors in experimental method and not the result of shortcomings of the numerical approach that they employed. The S-A turbulence model was noted to provide results which were in better agreement with the experimental data than the RKE model.

In this work, we develop an approach to model the flow around an isolated rotating front wheel of a bicycle in contact with the ground. Motivation to limit this study to consider just the front wheel of the bicycle is three-fold. First, this is the part of the bicycle that the wind sees first. We speculate that the aerodynamic performance of bicycle components behind the front wheel will be affected by events occurring upstream. Second, the drag associated with an individual rider, assuming that riding position has been optimized already, is dictated by the fixed size and shape of the rider; the design of the front wheel can still be optimized to improve overall performance and

handling characteristics. Finally, wind tunnel data is available for comparison with several individual wheel designs over a range of conditions typically encountered by racing cyclists.

II. Methodology

A. Wheel, Hub and Spoke Geometry

A profile gauge was used to measure the cross sectional profile of a standard Zipp 404 wheel (formerly Zipp Speed Weaponry, Indiana, USA) with a continental Tubular tire attached. The hub profile was also measured using the same method. The exact size and shape of the wheel and hub cross sections are shown in Figure 2. Elliptical spokes were measured using a caliper and the radius of curvature of the leading and trailing edges was estimated to be 0.5 mm. The geometry of time trial and triathlon bicycles places much of the weight of the rider directly over the front wheel through the use of aerobars. To obtain an estimate of the contact area between the road and the front tire, a bicycle (2005 Elite Razor, Elite Bicycles Inc., Pennsylvania, USA) was mounted on a training device, a 170lb rider was positioned on the bicycle, and the contact area of the deflected tire was traced. The contact area was standardized as part of the model geometry used in this study. Under actual riding conditions, variations in the road surface would lead to vertical translation of the wheel, thus varying the contact area. It is felt that a ground contact consideration is important, and that a standardized ground contact shape is a reasonable approximation.

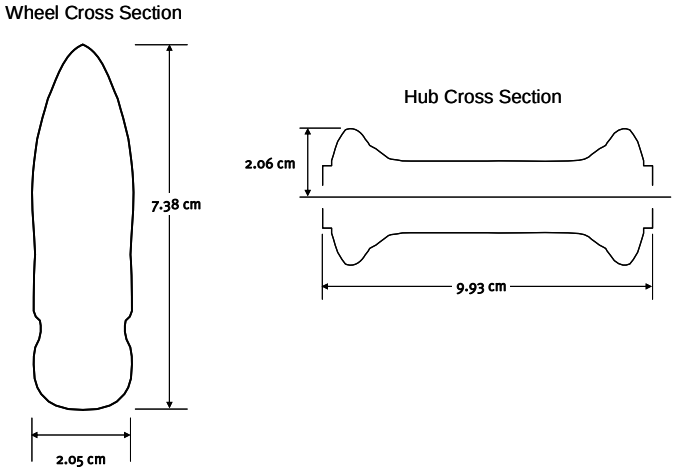

Figure 2: Wheel and Hub Cross Sectional Profiles

B. Computational Grid Development

The model domain was divided into two sub-volumes, with one containing the spokes, hub and inner edge of the wheel rim, and the other containing the remaining toroidal wheel surface, the ground contact and the surrounding volume. This approach makes it possible in future studies to replace individual components such as the wheel, and easily change other elements of the bicycle wheel geometry, such as the spoke count. This domain division also provides for application of a rotational frame of reference to the inner wheel section, permitting realistic movement of the spokes in transient modeling efforts. A well parameterized journal was developed using GAMBIT[19] to automatically generate the geometry and computational grids used in this work. The inner wheel section contained parameters to control the spoke count, spacing and the location of spoke attachment to the hub surface. A non-conformal interface was used between the inner wheel sub-volume and the surrounding fluid

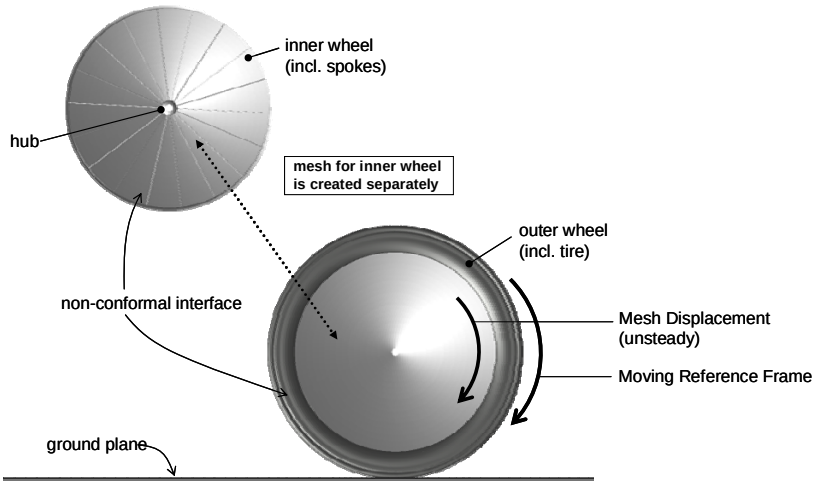

Figure 3: Methodology for meshing the wheel geometry

volume. An illustration of this methodology is shown in Figure 3. The yaw angle, specified as another parameter in the journal file, was used to correctly orient the complete wheel, including the inner wheel sub-volume, within the surrounding volume. Thus, the mesh created on the surface of wheel, hub and spokes, the mesh boundary layers applied to the wheel and components, and, the mesh generated for the inner wheel volume was identical for each yaw angle studied. Due to the change in location for the wheel and inner wheel sub-volume, there were slight changes in the mesh for the surrounding fluid mesh for each yaw angle. This approach permitted simplification of the upstream boundary conditions. Illustrations depicting the final mesh used in the studies and the actual geometry are shown in Figure 4. The baseline computational grid used in this work contained roughly 1M nodes and 5M tetrahedral elements. A small number of pyramid elements where used for the boundary layers. A coarser mesh with ~3.8M elements and 0.8M nodes, and a finer mesh with nearly 16M elements and ~3M nodes were developed to explore numerical grid accuracy. Element aspect and distortion ratios for surface triangles and tetrahedral volume elements were maintained well below the standard default limits specified by GAMBIT™.

Figure 4. Mesh near hub (top) and wheel (bottom) compared to the actual Zipp 404 wheel

C. Boundary Conditions

A uniform velocity profile was applied to the upstream boundary of the computational domain. This velocity was chosen to match the forward speed of the bicycle. For this work, speeds of 20mph and 30mph were applied as a uniform velocity profile on the upstream inlet. A constant eddy viscosity inlet condition was specified to be 0.001. The ground plane was modeled as a no-slip surface, with a constant translational velocity matching the specified upstream speed. The ground plane velocity components were parallel to the forward motion of the bicycle. Yaw angles spanning the range from 0 to 20 degrees were examined. For the RANS computations, a rotational frame of reference was applied to the outer wheel, inner wheel, spokes and hub using a rotational velocity which was consistent with the upstream velocity being studied. For the DDES computations, a rotational frame of reference was applied to the outer wheel as was done in the RANS case. On the inner wheel sub-volume, which contained the inner wheel rim, hub and spokes, a rotational mesh motion was applied to turn the wheel at a speed matching the outer wheel reference frame. A pressure outlet condition was applied to the downstream boundary of the model domain. Slip conditions were applied to the remaining outer boundaries of the surrounding volume. The extents of the computational domain were specified with respect to the wheel diameter, D. The wheel was placed at a distance of 0.75D from the constant velocity inlet plane. Other dimensions were arrived at after preliminary steady state simulations were run to confirm that the chosen extents were sufficient to resolve the external flow behavior surrounding the wheel. An illustration of these boundary conditions and the computational domain extents are illustrated in Figure 5.

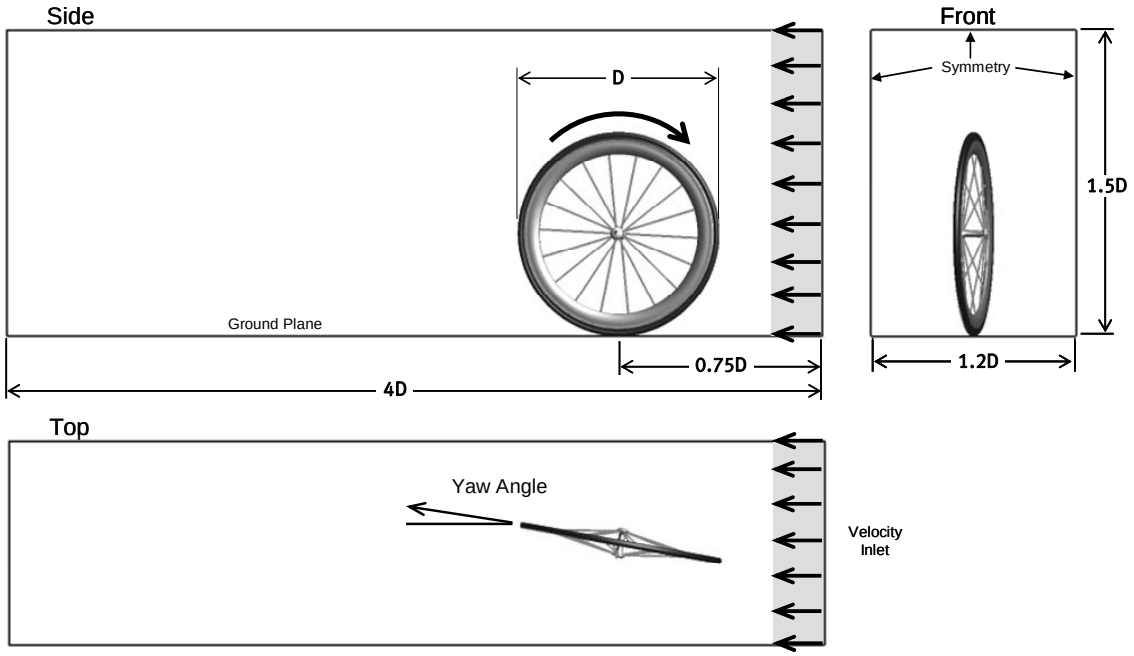

Figure 5: Boundary Conditions and Wheel Position within the Computational Domain

D. Numerical Methodology

In this work, the Navier-Stokes equations were solved using *AcuSolve*™, a commercially available flow solver base on the Galerkin/Least-Squares (GLS) finite element method[20,21,22]. *AcuSolve*™ is a general purpose CFD flow solver that is used in a wide variety of applications and industries. The flow solver is architected for parallel execution on shared and distributed memory computer systems and provides fast and efficient transient and steady state solutions for standard unstructured element topologies. Additional details of the numerical method are summarized by Johnson et.al.[23].

The GLS formulation provides second order accuracy for spatial discretization of all variables and utilizes tightly controlled numerical diffusion operators to obtain stability and maintain accuracy. In addition to satisfying conservation laws globally, the formulation implemented in *AcuSolve*™ ensures local conservation for individual elements. Equal-order nodal interpolation is used for all working variables, including pressure and turbulence equations. The semi-discrete generalized-alpha method[24] is used to integrate the equations in time for transient simulations. The resultant system of equations is solved as a fully coupled pressure/velocity matrix system using a preconditioned iterative linear solver. The iterative solver yields robustness and rapid convergence on large unstructured meshes even when high aspect ratio and badly distorted elements are present.

The following form of the Navier-Stokes equations were solved by *AcuSolve* ™ to simulate the flow around the bike wheel:

$$\frac{\partial \rho}{\partial t} + \nabla \cdot \rho \mathbf{u} = 0 \qquad \textbf{(1)}$$

$$\rho \frac{\partial \mathbf{u}}{\partial t} + \rho \mathbf{u} \cdot \nabla \mathbf{u} + \nabla p = \nabla \cdot \tau + \rho \mathbf{b} \qquad \textbf{(2)}$$

Where: ρ=density, **u** = velocity vector, p = pressure, **τ** = viscous stress tensor, **b**=momentum source vector.

Due to the low Mach Number (Ma ~ 0.04) involved in these simulations, the flow was assumed to be incompressible, and the density time derivative in Eq. (1) was set to zero. For the steady RANS simulations, the single equation Spalart-Allmaras (SA) turbulence model[17] was used. The turbulence equation is solved segregated

from the flow equations using the GLS formulation. A stable linearization of the source terms is constructed to provide a robust implementation of the model. The model equation is as follows:

$$\frac{\partial \tilde{\nu}}{\partial t} + \mathbf{u}\cdot\nabla\tilde{\nu} = c_{b1}\tilde{S}\tilde{\nu} - c_{w1}f_w\left[\frac{\tilde{\nu}}{d}\right]^2 + \frac{1}{\sigma}\left\{\nabla\cdot\left[(\nu+\tilde{\nu})\nabla\tilde{\nu}\right] + c_{b2}(\nabla\tilde{\nu})^2\right\} \qquad \textbf{(3)}$$

$$\tilde{S} = |S| + \frac{\tilde{\nu}}{\kappa^2 d^2} f_{v2} \qquad f_{v2} = 1 - \frac{\chi}{1+\chi f_{v1}}$$

$$g = r + c_{w2}(r^6 - r) \qquad f_{v1} = \frac{\chi^3}{\chi^3 + c_{v1}^3}$$

$$\chi = \frac{\tilde{\nu}}{\nu} \qquad S_{ij} = \frac{1}{2}\left(\frac{\partial u_i}{\partial x_j} + \frac{\partial u_j}{\partial x_i}\right) \qquad f_w = g\left[\frac{1+c_{w3}^6}{g^6 + c_{w3}^6}\right]^{\frac{1}{6}}$$

$$r = \frac{\tilde{\nu}}{\tilde{S}\kappa^2 d^2} \qquad |S| = (2S_{ij}S_{ij})^{1/2}$$

Where: $\tilde{\nu}$ =Spalart-Allmaras auxiliary variable, d=length scale, c_{b1} = 0.1355, σ=2/3, c_{b2} = 0.622, κ=0.41, c_{w1} = c_{b1}/κ^2+ $(1+c_{b2})/\sigma$, c_{w2} = 0.3, c_{w3}=2.0, c_{v1}=7.1.

The eddy viscosity is then defined by:

$$\nu_t = \tilde{\nu} f_{v1}$$

For the steady state solutions presented in this work, a first order time integration approach with infinite time step size was used to iterate the solution to convergence. Steady state convergence was typically reached within 20 to 35 time steps for most simulations. Yaw angles above 14 degrees require small amounts of relaxation to obtain numerical convergence.

For the transient simulations, the Delayed Detached Eddy Simulation (DDES) model was used[25]. This model differs from the (SA) RANS model only in the definition of the length scale. For the DDES model, the distance to the wall, **d**, is replaced by $\tilde{d}$ in Eq. (3). This modified length scale is obtained using the following relations:

$$r_d = \frac{\nu_t + \nu}{\sqrt{u_{i,j}u_{i,j}}\kappa^2 d^2} \qquad f_d = 1 - \tanh([8r_d]^3) \qquad \tilde{d} = d - f_d \max(0, d - C_{DES}\Delta)$$

Where: Δ=local element length scale, and C_{DES} = the des constant.

This modification of the length scale causes the model to behave as RANS within boundary layers, and similar to the Smagorinsky LES subgrid model in separated flow regions. Note that the above definition of the length scale deviates from the original formulation of DES, and makes the RANS/LES transition criteria less sensitive to the mesh design.

Transient simulations in this work were carried out for several yaw angles at speeds matching the steady runs . Calculations were run for two full rotations of the bicycle wheel, with simulation results saved at every 2^o of wheel rotation. In subsequent frequency analyses of the resolved forces, only the last 256 time steps for each transient case were used since it was noted that the numerical solution required some time steps in order to be stabilized.

E. Scope of Work and Force Resolution

The scope of this work encompassed the study of 10 different yaw angles (0^o, 2^o, 5^o, 8^o, 10^o, 12^o, 14^o, 16^o, 18^o and 20^o) at the two speeds of 20mph and 30mph, resulting in 20 individual design points run at steady state. Based on these results, transient studies were then run for 5 different yaw angles (0^o, 2^o, 5^o, 10^o and 20^o) at the same two speeds, generating solution results for 256 time steps for each case – this produced at total of 2560 solutions to be analyzed. Because of the repetitive and quantitative nature of the calculations required, postprocessing of the simulation results to resolve drag, side and vertical forces, and generate reports, was automated through the use of the FVX™ programming language feature available with FieldView[26].

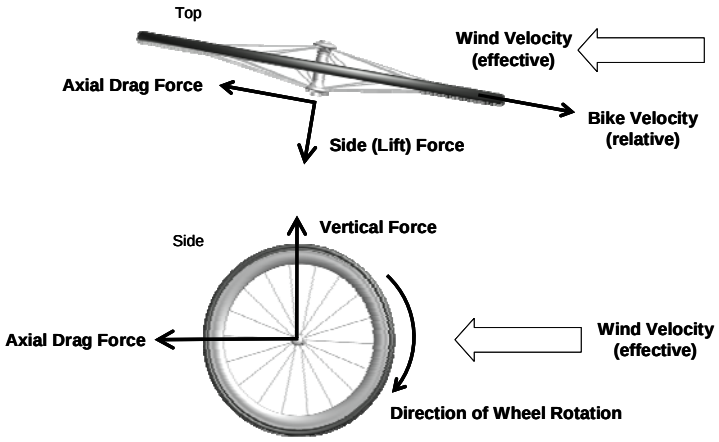

Figure 6: Force Resolution on the rotating bicycle wheel

Pressure and viscous forces were resolved to match: A) the axial drag force that a cyclist would experience in opposition to the direction of motion; B) the side (or lift) force, acting in a direction perpendicular to the direction of motion, and finally; C) the vertical force acting either towards or away from the ground plane, again acting perpendicular to the direction of motion. An illustration of the resolved forces with respect to the orientation of the bicycle wheel is shown in Figure 6. Also illustrated are the effective bicycle velocity and the effective wind velocity vectors which would represent the experimental conditions consistent with wind tunnel testing.

Resolved forces were further broken down to permit comparison of the separate contributions from the wheel itself (including the tire and rim), the hub, and all of the spokes. A further calculation was carried out on just the wheel to examine the circumferential variation of the resolved forces. This was accomplished by computing the resolved force components on a circular segment spanning 1^o, repeated to encompass the entire 360^o circumference of the wheel.

III. Results

A. Resolved Forces for RANS calculations

At all speeds and yaw angles studied, the contributions from viscous drag were seen to be less than 3% of the overall force. From a practical standpoint, virtually all of the forces computed are a result of pressure drag. The resolved drag, side (or lift) and vertical forces, summarized, and broken into component contributions for the wheel, spokes and hub, are shown in Figures 7 thru 9. At 0^o yaw, the drag coefficients, C_D, calculated for 20mph and 30mph, were **0.0308** and **0.0311,** respectively. This is in very good agreement with the results of Greenwell et al.[4] who reported a drag coefficient for a similar wheel (HED CX, Hed Cycling Products, Shoreview MN, USA) of **0.0389** and with Tew et al.[8] who reported a drag coefficient in the range of **0.0280** to **0.0300** for another wheel of very similar design (Campagnolo SHAMAL, Campagnolo S.r.l., Vicenza, Italy) to the Zipp 404 model studied here.

In Figure 7 we observed a delayed increase in the drag force as the yaw angle increased. The delayed onset of increasing drag force with increasing yaw angle is also seen to qualitatively match the experimental results of Greenwell et.al.[4] and Kuhnen[27], who summarized drag forces as a function of yaw angle for several commercial racing wheels. From the component breakdown, it is seen that the wheel itself is responsible for most of the drag force at both speeds studied. The spokes, while very small in terms of projected area, do account for drag forces which are comparable to those observed on the hub.

Experimental results for the side force are observed to generally increase in a nearly linear fashion with respect to increasing yaw[4,8]. In Figure 8 we also observed this trend and the side force coefficients calculated in this work again match reasonably well with the experimentally published wind tunnel measurements. Side force coefficients

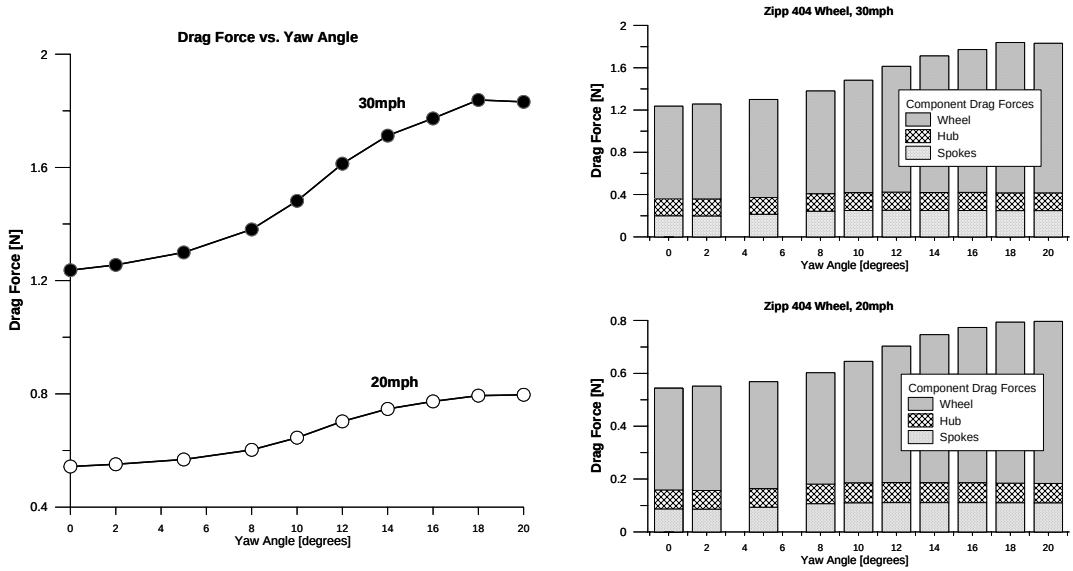

Figure 7: Axial Drag force (on left) and component summary (on right) as a function of Yaw angle

for the HED CX at 30mph and the SHAMAL at 55kph, both at 20^o yaw, were **0.32** and **0.30**, respectively. In this work, side force coefficients were reported the same for 20mph and 30mph and 20^o yaw as **0.23.** Side force contributions are strongly dominated by the wheel component, with the hub contributing the least to overall side forces.

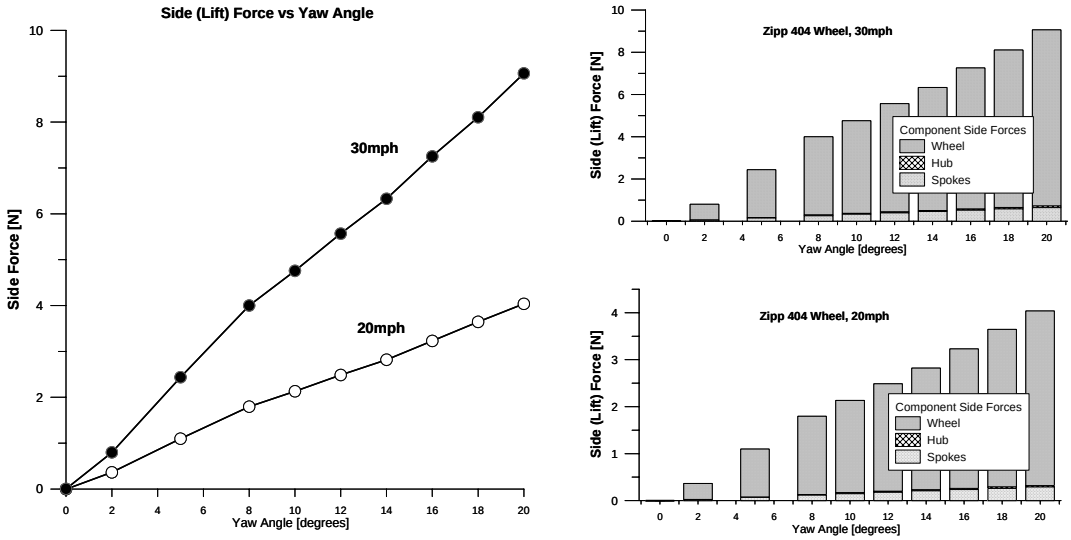

Figure 8: Side (or Lift) force (on left) and component summary (on right) as a function of Yaw angle

Vertical forces, shown in Figure 9, have not been reported for wind tunnel studies. In our calculations we note an interesting and unexpected transition where the vertical forces switched from acting downward to acting upward at a yaw angle between 5 to 8 degrees. This result is consistent with anecdotal observations of cyclists who have experienced control and maneuverability issues when riding in crosswind conditions. An examination of the component forces acting on the hub, spokes and wheel reveals that only the wheel is seen to exhibit this transitional behavior. Notably, the forces on the hub are seen to follow the well established Kutta-Joukowski theorem (or Magnus[28] effect) for 'lift' generated by a rotating cylinder. As calculated by Glauert[29], the vertical forces are seen to always act downward on the hub for all yaw angles considered.

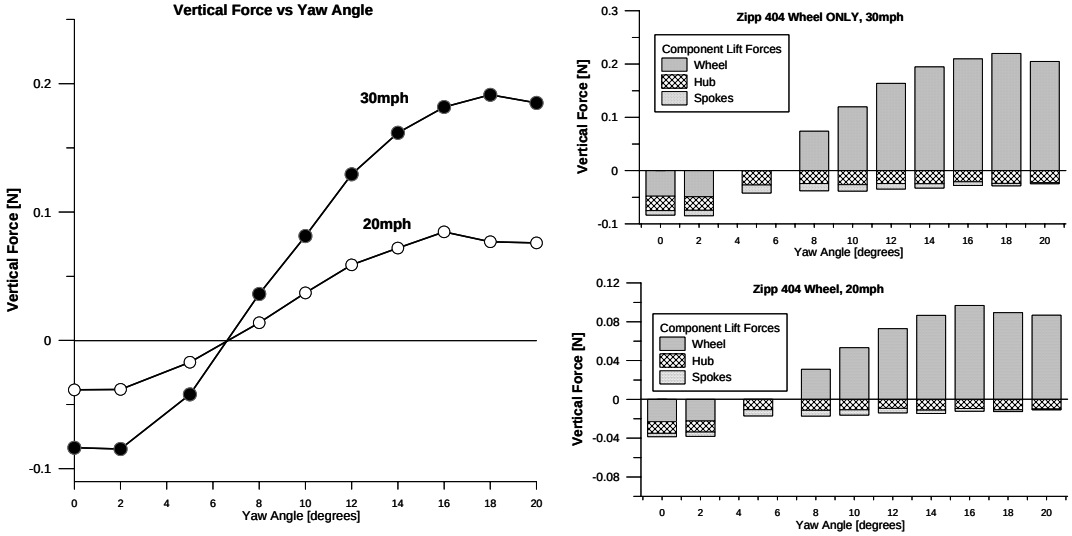

Figure 9: Vertical force (on left) and component summary (on right) as a function of Yaw angle

To better understand the resolved forces acting on the wheel alone, calculations were carried out for small circular arc segments, averaged over 1^{o} of arc, and are plotted as a function of the wheel circumference in Figures 10, 11 and 12. The effective wind velocity moves from right to left, and the leading edge of the wheel is at a circumferential measure of 0 degrees. The ground contact and top of the wheel are at 90 and 270 degrees, respectively. For the case of drag forces, we see that the highest value for drag occurs on the leading edge of the wheel. At the top and bottom of the wheel, the drag forces are seen to be essentially zero, which is expected.

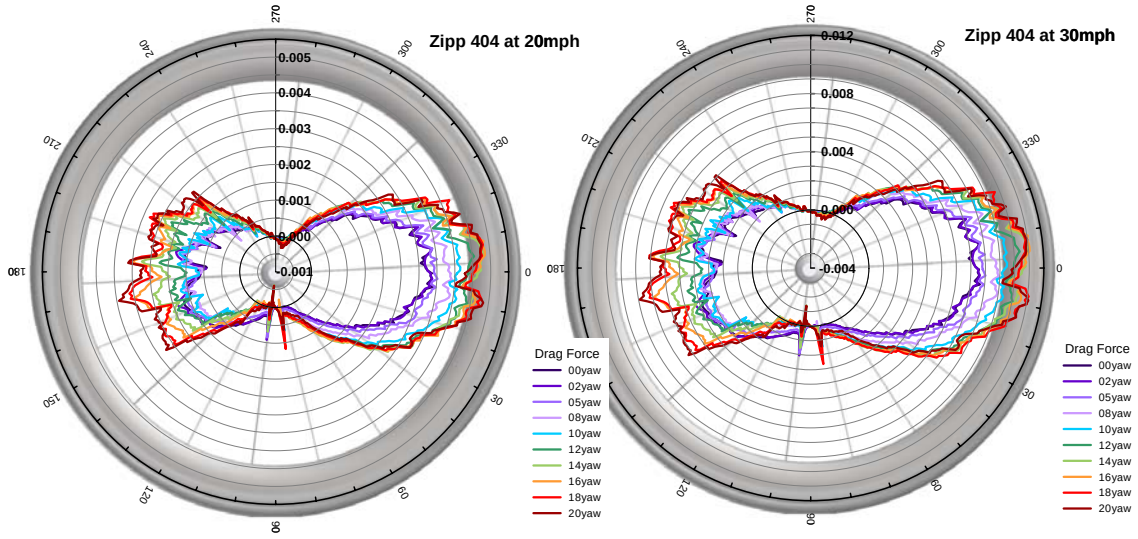

Figure 10: Circumferential Variation in Drag Force at 20mph (left) and 30mph (right)

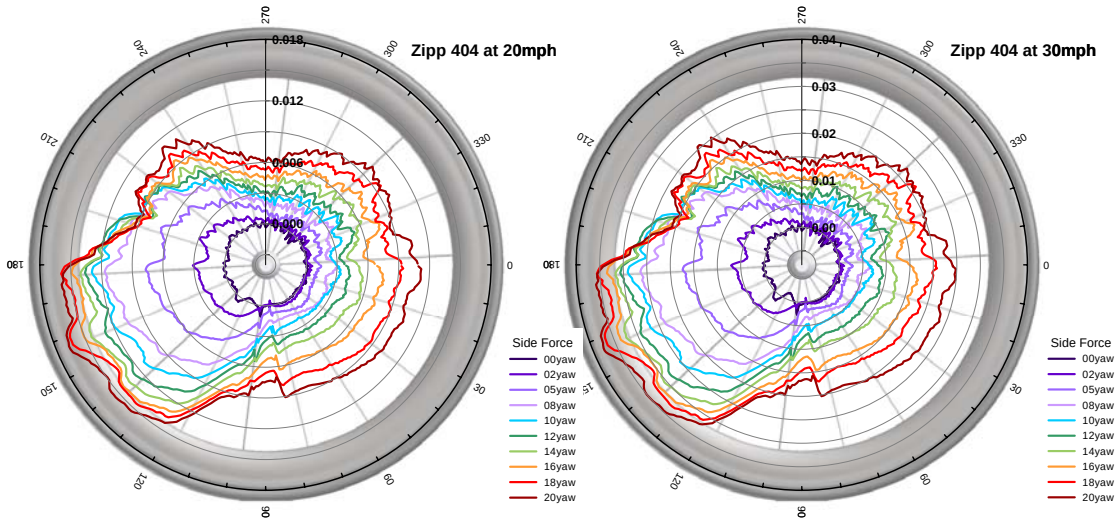

Figure 11: Circumferential variation in side force at 20mph (left) and 30mph (right)

The side forces, shown in Figure 11 are seen to be greatest on the trailing edge of the wheel for all yaw angles studied. Trends for both speeds appear to be similar. The build-up of side forces on the trailing part of the wheel is expected to play a role in terms of handling and maneuverability.

The vertical forces, shown in Figure 12, again exhibit similar trends at both speeds. In both cases, we observed a large positive vertical force (acting upwards) in the leading lower portion of the wheel, and, a similar region of positive vertical force acting on the trailing upper edge of the wheel. At the lower yaw angles, these positive regions appear to be offset by the downward acting forces, and as was seen in Figure 9, at a yaw angle between 5^{o} and 8^{o}, a transition occurs.

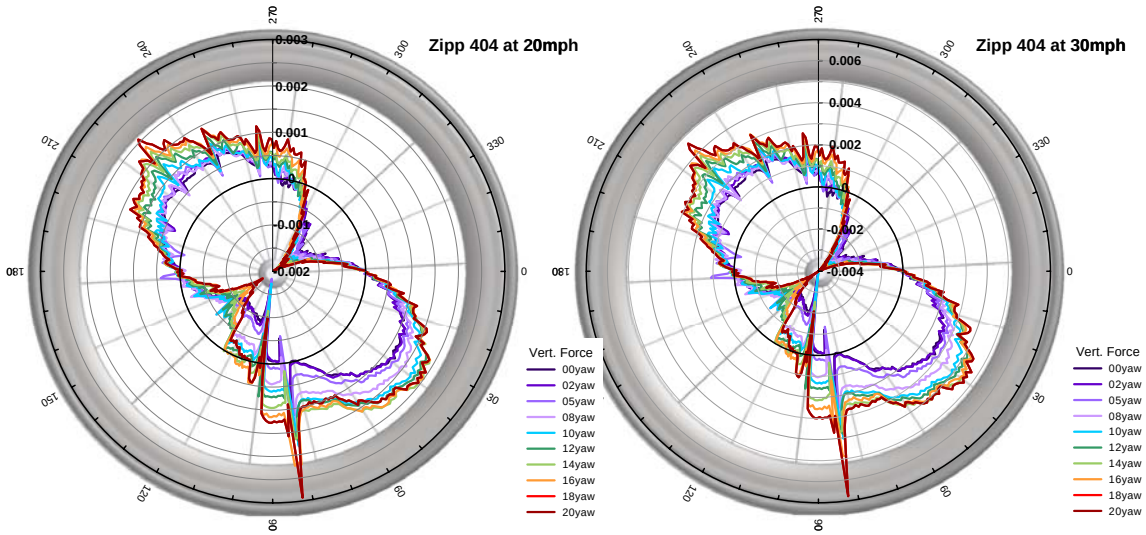

Figure 12: Circumferential variation in vertical force at 20mph (left) and 30mph (right)

B. Resolved Forces for DDES Calculations

The resolved drag, side (or lift) and vertical forces, for the whole wheel, including the wheel rim, hub and spokes, calculated over the last 256 time steps for each yaw angle, are illustrated in Figures 13, 14 and 15.

In all the time history plots, the time on the bottom abscissa was represented in non-dimensional form (***t**** = ***tV/D***), where D was set equal to the wheel diameter and V was set equal to the nominal bike speed The axis on the top of the plot represents the rotational angle of the wheel; 720 degrees is equal to two full wheel rotations. Drag, side and vertical force coefficients were standardized using a reference area ($S = \pi D^2/4$) consistent with that used by Greenwell et al.[4] and Tew et al.[8] In order to show the smaller variations in the drag, side and vertical forces at the lower yaw angles, an expanded ordinate scale on the right side of each time history plot was used to display the cases corresponding to 0°, 2° and 5° yaw. Power spectral densities were computed using Fourier transforms for each resolved force, for each yaw angle, and are shown, plotted against the Strouhal number, **St**, $St = fD/V$.

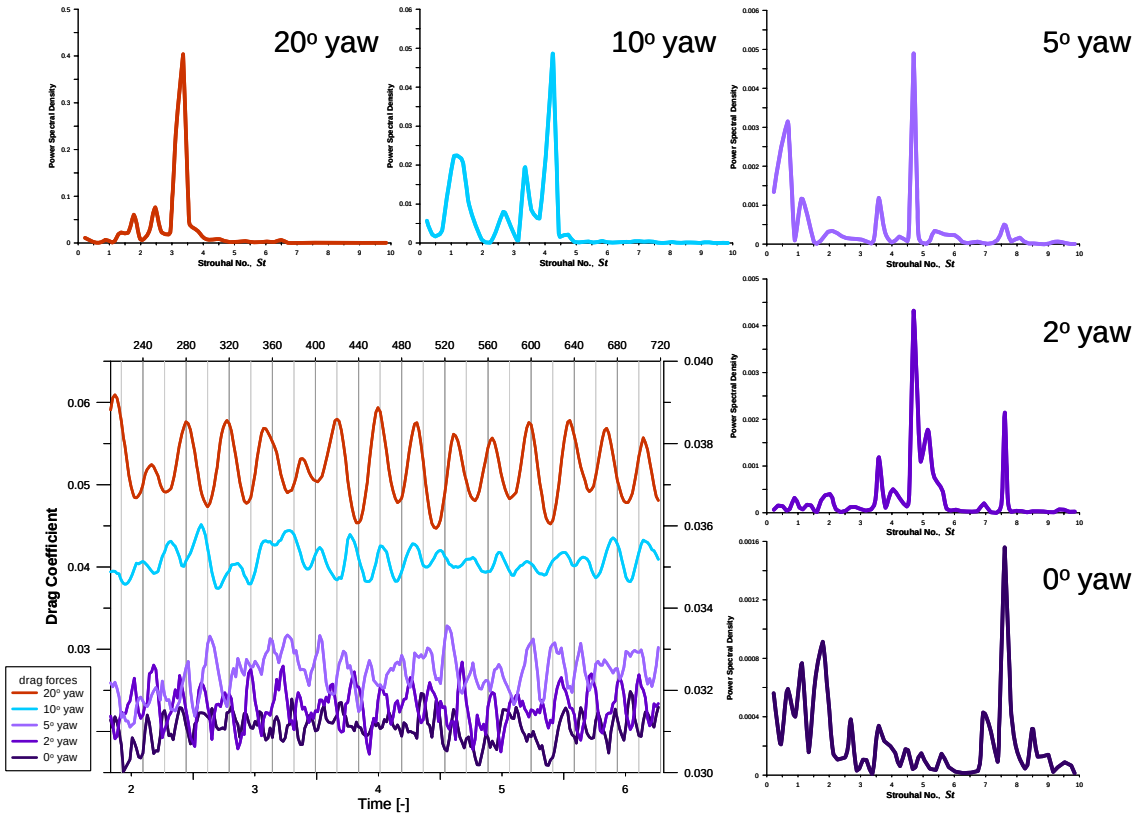

Figure 13: Drag Force versus time and Power Density Spectra for all Yaw angles at 20mph

For the time period studied, we observed that for the lowest shedding frequency (which corresponds to the highest yaw angle of 20°), we have captured 15 cycles for the drag and side force coefficients. The vertical force was seen to be smaller in magnitude than either of these forces. As a result an observation of the number of cycles based on the time history results was not reported. For the resolved drag force at 0° yaw, we observed a dominant peak at a Strouhal number of St = 7.61 which was significantly reduced at 2° and 5° yaw, and was no longer present at higher yaw angles. At 2° and 5° yaw, another dominant peak was observed at St = 4.70. At 10° and 20° yaw, this peak shifted to St = 4.24 and St = 3.36 respectively. With the exception of 0° yaw, these same dominant peaks were also observed for computations based on the side force. At 0° yaw, a dominant peak for the side force was observed at St = 4.92. Computations based on the vertical forces exhibited higher frequency peaks for St = 7.61 at 0° and 2° yaw, similar to those computed from the drag forces. Some weaker peaks consistent with observations for the drag and side forces at St = 4.70 and St = 3.58 were also seen. For all yaw angles examined, a strong low frequency peak was resolved from the vertical forces at a St = 0.67, however the meaningfulness of this observation is questionable due to low signal strength for this vertical force component and insufficient temporal resolution.

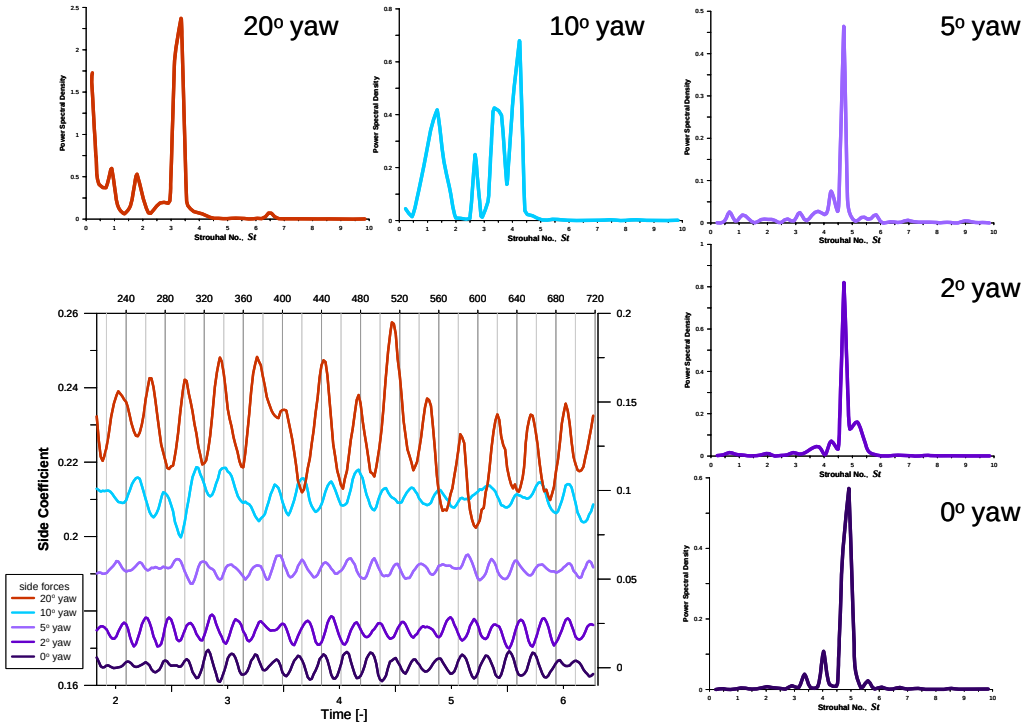

Figure 14: Side Force versus time and Power Density Spectra for all Yaw angles at 20mph

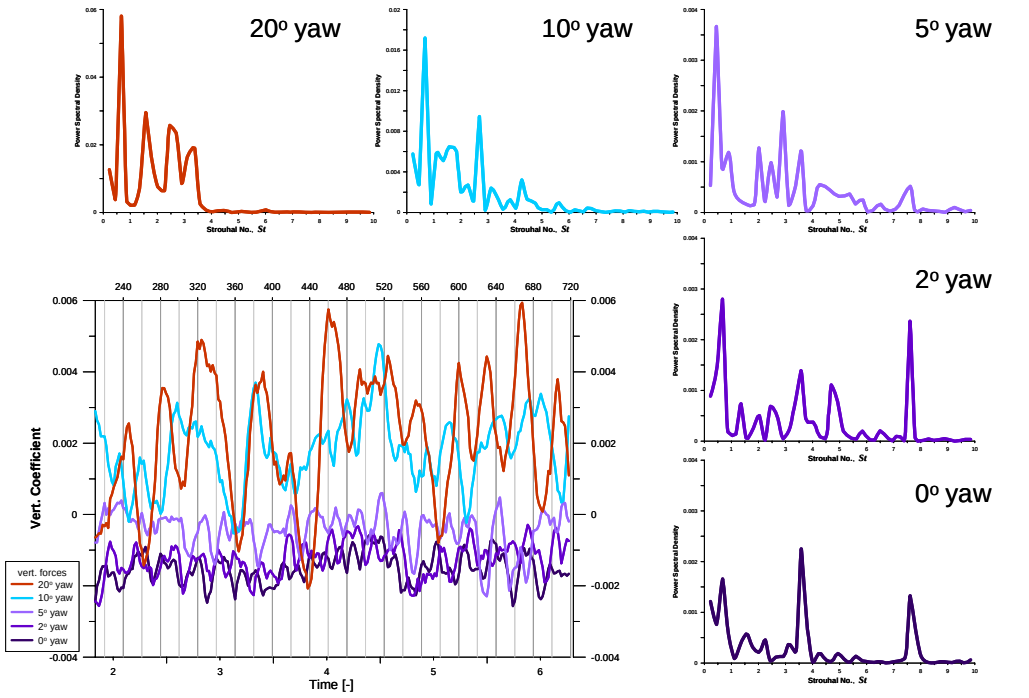

Figure 15: Vertical Force versus time and Power Density Spectra for all Yaw angles at 20mph

It is notable that none of the peaks observed for any of the resolved forces matched the frequency of the passage of the rotating spokes. Considering all 18 spokes, the matching Strouhal No. was St = 5.73. If just one side of the wheel is considered, then the corresponding Strouhal No, for the passage of the 9 spokes, is St = 2.86. Neither of these frequencies were observed for any yaw angles.

Since the wheel itself was previously noted to be the main contributor to all the resolved forces, frequency analyses were carried out on just the wheel itself. Also, frequency analyses were carried out on the hub in an attempt to make comparisons to known results for transient flows past circular cylinders. A summary of the Strouhal number peaks observed from the analyses on the wheel and hub is presented in Table 1. For the wheel, the characteristic dimension used to calculate the Strouhal number was the wheel diameter, D. For the hub, an average hub diameter was used. In some cases, the frequency analyses on the hub did not return a distinctive peak. A partial reason for this problem is that the flow around the hub was likely disrupted significantly by vortex shedding from the upstream leading edge of the wheel. Resolution of peaks was also more difficult when computations were based on the weaker vertical forces.

	yaw	Wheel		Hub	
		20mph	30mph	20mph	30mph
drag	0°	3.58	3.58	--	--
	2°	3.58	4.92	0.195	0.195
	5°	4.70	4.70	0.195	0.195
	10°	4.25	4.25	0.176	0.176
	20°	3.36	3.36	0.139	0.139
side	0°	4.92	4.92	0.204	0.204
	2°	4.70	4.70	0.195	0.195
	5°	4.70	4.70	0.195	0.195
	10°	4.25	4.25	0.176	0.176
	20°	3.36	3.36	0.139	0.139
vertical	0°	3.58	3.58	0.148	--
	2°	4.92	4.70	0.148	--
	5°	4.70	4.70	0.195	0.195
	10°	--	--	0.176	0.176
	20°	3.36	3.36	0.129	0.139

Table 1: Strouhal Numbers for Wheel and Hub

In general, dominant frequencies obtained for each of the resolved forces were seen to be the same for matching yaw angles for both speeds studied. Also, it was observed that the frequencies for the wheel and the hub had a tendency to decrease as the yaw angle increased. This was consistent with observations made for the resolved forces, summed for all wheel components. A direct comparison of the Strouhal number observed for the hub in this work with that reported for a cylinder of constant cross section in an unobstructed flow is encouraging. Chew et al.[30] reported a Strouhal No. computed from numerical simulations, of approximately St = 0.22 for a cylinder with a free stream Re = 34000, rotating at the same peripheral velocity as the free stream velocity. These conditions were considered to be quite comparable to the hub, where Re = 25800 at 30mph. Labraga et al.[31] reported very similar results experimental results (again, St = 0.22) obtained from LDA and PIV studies.

C. Flow Features

The transient DDES results were used to visualize flow features. Results obtained at 20mph were qualitatively similar to those for 30mph. In Figure 16a, b, c and d, a series of helicity contours are shown for each yaw angle studied at 20mph. Helicity values were computed from the instantaneous flow field for the last time step computed in the transient analyses. Planes within each of the four series were taken at the same angle along the wheel circumference, and were re-oriented to be displayed normal to the circumferential angle. A circumferential angle of 0 degrees represents the leading edge of the wheel, while 270 and 90 degrees represent the top and bottom of the wheel, respectively. In Figure 16a, the angular plane at 266 degrees corresponds to a position just behind the top of the wheel. At this position, as the yaw angle increased, we observed a clockwise (as viewed from behind the wheel) vortex coming off of the outer edge of the wheel, and a counterclockwise vortex coming off of the inner edge of the wheel rim on the suction side. Both vortices, once separated were seen to move in a downstream direction, being carried along by the surrounding axial flow. In Figure 16b, the angular plane was moved forward to 340 degrees, closer to and above the leading edge of the wheel. Again, a pair of counter-rotating vortices were noted, coming off of the inner and outer edges of the wheel. These vortices were carried along with the forward rotation of the wheel and were continually shed along the circumference of the wheel as seen in Figures 16b and 16c. Downstream from the ground contact, at an angular position of 108 degrees these shedded vortices were once again seen to be carried along with the surrounding flow.

In order to develop an understanding of the evolution of these flow structures, streaklines were calculated for each of the yaw angles simulated at 20mph. A seeding pattern was created to release massless particles very near to

the surface of the wheel on either the pressure side or the suction side. Figure 17a shows the trajectories of massless particles seeded near the surface of the wheel on the pressure side, after 100 time steps following their initial release.

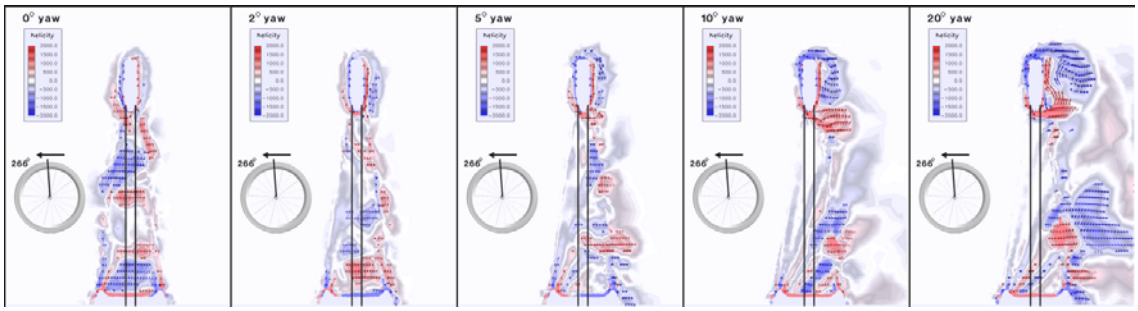

Figure 16a: Helicity plots at 266 degrees along the wheel

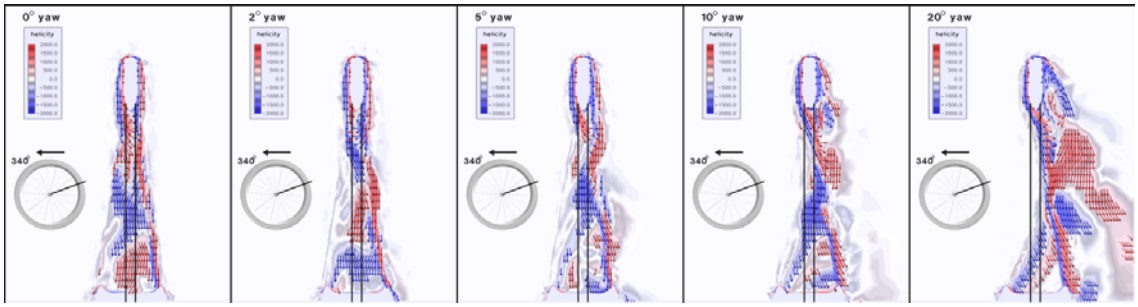

Figure 16b: Helicity plots at 340 degrees along the wheel

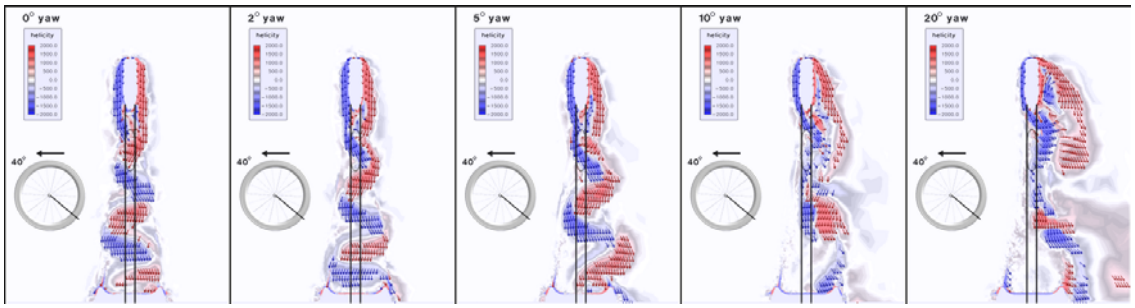

Figure 16c: Helicity plots at 40 degrees along the wheel

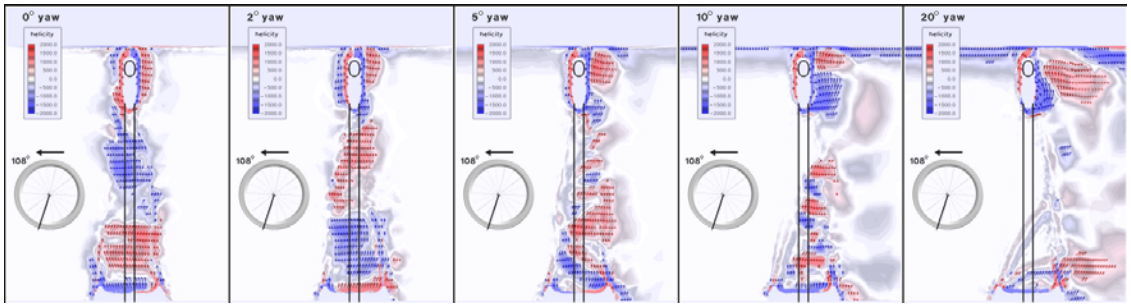

Figure 16d: Helicity plots at 108 degrees along the wheel

The massless particles were colored by the lateral velocity component perpendicular to the axial flow. Figure 17b shows the trajectories of massless particles seeded on the suction side of the wheel, again for all yaw angles simulated for 20mph.

From these illustrations, several flow structures can be identified. At the top of the wheel for all yaw angles studied, we observed a vortex resulting from collision of air being dragged forward by the outer edge of the surface of the rotating wheel into the oncoming free stream flow. At a 0^o yaw angle, this vortex structure was seen to be oriented nearly vertically at an angular position of 270 degrees, at the top of the wheel. As the yaw angle increased, the axis of this vortex tilted, becoming more horizontal.

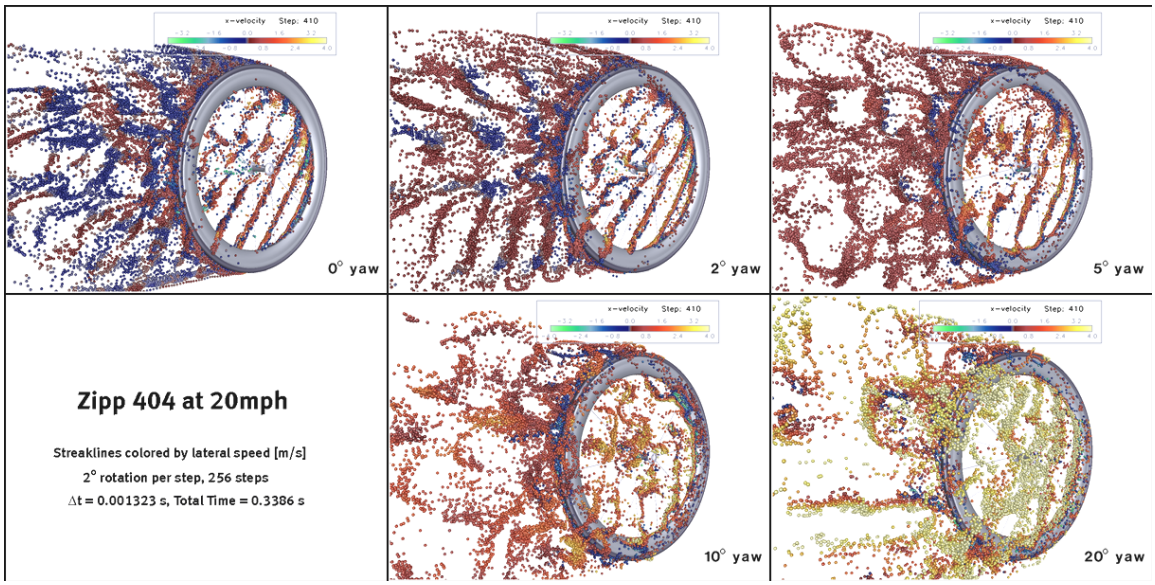

Figure 17a: Streaklines released on the pressure side of the wheel

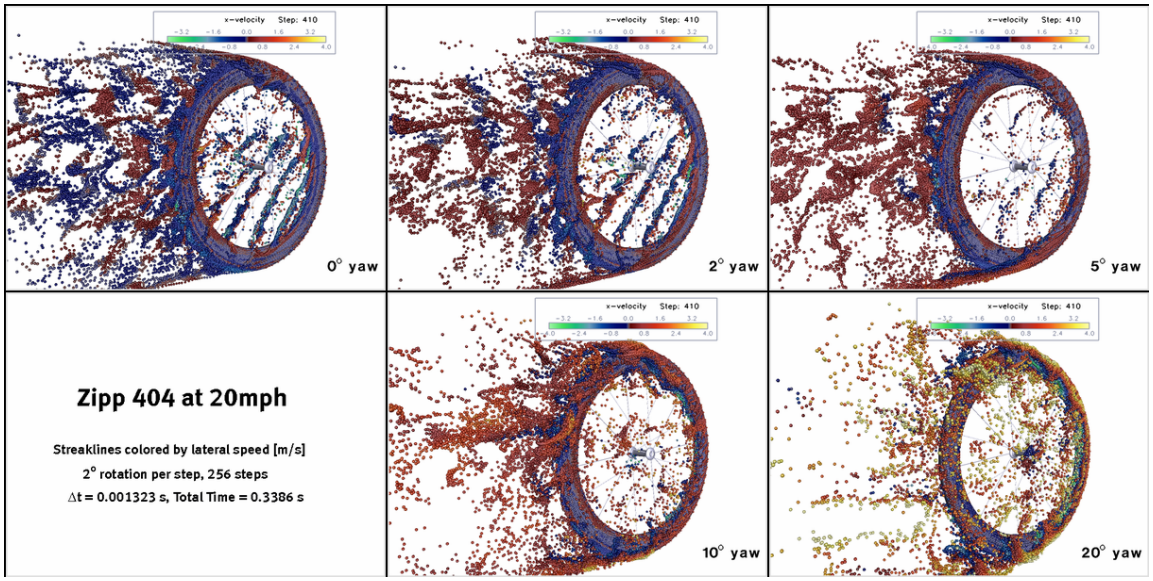

Figure 17b: Streaklines released on the suction side of the wheel

In Figure 17a, we observed a strong alignment of the massless particles, rolled into nearly straight structures, at an angle sloping upward towards the top of the wheel, for the cases of 0^o, 2^o and 5^o yaw angles. We speculate that this structure is created by the fluid being dragged forward at the inner edge of the leading section of the wheel rim, which eventually sheds off the wheel. We speculate that the reasoning behind why these structures appear nearly straight is related to the speed difference between the wheel and the approaching air. On the upper leading quadrant

of the wheel, the difference between the linear wheel speed is a maximum at 270 degrees (or the top of the wheel) and decreases to a minimum for this leading quadrant at 0 degrees (or the front of the wheel). Going from the front of the wheel down to the ground contact at 90 degrees, the difference between the wheel speed and the oncoming air continues to decrease. At the ground contact, the wheel speed and the ground plane are moving at the same speed; the difference in flow speed is zero. In the upper quadrant of the wheel, shedding from the inner rim occurs sooner due to the higher difference between the linear wheel velocity and the oncoming air. As this velocity difference becomes less, the shedding of the vortex from the inner rim is delayed. We believe that this delay in vortex shedding is the phenomena responsible for the aligned rows of massless particles. We further observed that the timing between the shedding structures was the lowest at 0^o and increased as the yaw angle increased. Above a yaw angle of 5^o the "straight" aligned flow structures were seen to break up. It is believed that the well aligned flow structures evolved from vortex shedding, initiated at the centerline of the wheel rim, and that at higher yaw angles, massless particles were not in position to be able to visually resolve this phenomenon. These structures were observed to be less prominent when streaklines were released from the suction side of the wheel as illustrated in Figure 17b. Again, it is felt that streakline particles had already moved away from the centerline of the wheel, having started on the suction side, and were not in a position to resolve this flow structure.

In the upper quadrant of the wheel, flow passing the outer edge of the wheel was seen to either join the vortex already identified, or, to be dragged along downwards following the rotational motion of the front wheel. As the yaw angle increased, this vortex was seen to roll down along front of the wheel, eventually extending from the upper quadrant of the wheel down to a point just ahead of the ground plane. The inner rim vortex described in the preceding paragraph was observed to lie underneath this outer vortex, rotating in the opposite direction. At higher yaw angles, the shedding of this outer edge vortex became the dominant flow structure.

Along the trailing rear quadrant of the wheel, another pair of counter-rotating vortices were observed, with one being generated by interaction of the flow being pulled along the inner edge of the and the oncoming air, and the other resulting from the flow on the outer edge of the wheel meeting the oncoming air. Flow in this are of the wheel was observed to be highly disrupted, in part due to the shedding of vortices from the upstream quadrants of the wheel.

D. Grid Resolution

To examine the influence of mesh resolution on the results, two grids, one of coarser mesh density, and one of finer mesh density than the baseline mesh were examined. Care was exercised to ensure that y+ values were maintained within reasonable ranges for each of the meshes studied.

The baseline mesh contained 1.06M nodes and 5.27M tetrahedral elements. There were some small variations in the total number of nodes and elements for differing yaw angles owing to small discretization differences in the surrounding volume around the wheel and inner wheel. The coarse mesh contained 0.8M nodes and 3.86M elements, while the fine mesh contained 2.85M nodes and 15.8M elements. Comparisons were made for resolved forces for 0^o and 10^o yaw angles. For the 0^o yaw case, comparisons were limited to drag and vertical forces only since the side forces were essentially zero for this case. The results of the comparisons are show in Table 2. In general, there were larger differences observed between the coarse mesh and the baseline mesh when compared to differences between the fine mesh and the baseline mesh. For the fine mesh, differences were seen to be very small in magnitude relative to the baseline mesh. Owing to the considerable number of calculations performed for each yaw angle (and over a range of time steps), it was felt that the baseline mesh provided sufficient spatial resolution to obtain reasonably accurate results.

		0^o yaw		10^o yaw	
		coarse	fine	coarse	fine
drag	pressure	-3.98%	1.34%	-2.47%	0.25%
	viscous	-1.28%	0.41%	-1.04%	-0.01%
	total	-4.06%	1.37%	-2.51%	0.24%
side	pressure	--	--	-4.36%	7.26%
	viscous	--	--	-0.65%	0.00%
	total	--	--	-4.37%	1.29%
vertical	pressure	2.02%	-6.96%	2.39%	-0.13%
	viscous	4.59%	1.17%	9.06%	0.01%
	total	1.97%	-0.13%	2.34%	-0.07%

Table 2: Grid Resolution Comparison

IV. Discussion

In this work CFD was used to explore the complex and unsteady nature of air flow around a rotating, isolated bicycle wheel in contact with the ground. A novel methodology using a sliding mesh with a non-conformal interface was introduced to resolve the problem of accurately modeling the movement of the spokes. Realistic ground plane and upstream boundary conditions were used to study an existing commercially produced bicycle wheel (Zipp 404). Steady and unsteady computations were performed using the commercial solver, *AcuSolve™*, over a range of speeds and yaw angles. From these results, automated methodologies were developed using FieldView FVX™ scripts to handle the repetitive tasks of i) resolving the pressure and viscous forces on the wheel into axial drag, side (or lift) and vertical components, ii) breaking the resolved forces into component contributions, iii) calculating the resolved forces along the wheel circumference, iv) preparing and reformatting the computed forces for seamless transfer into other software packages for further analysis, v) computation of streaklines and vi) visualization and animation of streaklines. In most instances, a newly conceived concurrent methodology involving the simultaneous execution of GAMBIT journal files, *AcuSolve™* solver runs and FieldView FVX™ scripts was used to substantially increase the throughput of data analysis for this work.

Agreement with the previously published wind tunnel results of Greenwell et al.[4] and Tews et al.[8] for resolved axial drag and side force or lift components was seen to be very good for both the steady and unsteady calculations. In this work, we present resolved forces acting in the vertical direction for the first time. We observed a transition from the expected downward acting force to the upward direction at a yaw angle between 5 and 8 degrees. By breaking the resolved forces down into individual contributions from the wheel, hub and spokes, something which is not possible with wind tunnel testing, and which is also being presented for the first time here, we have been able to link this unexpected transition to be limited to just the wheel. The hub was seen to act as expected in terms of the direction of vertical force, following the well known Kutta-Joukowski theorem. We believe that the transitional vertical force observation for the wheel alone may have a very significant impact upon the interpretation of more recent wind tunnel test results for bicycle wheels having deeper rim cross sections than that of the Zipp 404 modeled in this work.

Non-dimensional analyses of the resolved force coefficients showed only small differences between the speeds of 20mph and 30mph. Further, qualitative visualizations and frequency analyses showed very little difference between the two speeds examined. However, the absolute magnitude of forces computed is quite significant, as expected, and experimental wind tunnel studies which do not report differences with respect to wind speed should be considered suspect.

Transient studies of the rotating wheel revealed several new discoveries. We first note that the spokes play only a small role in terms of their contribution to the resolved forces and have no impact on the frequency of vortex shedding from the wheel. To fully resolve the role that the spokes play in the determining the performance of a racing bicycle wheel, simulations should be carried out with a range of spoke counts.

The frequency analyses of the resolved forces for the wheel indicated the presence of a periodic phenomenon at a Strouhal No. of St = 7.61 at 0^o and 2^o yaw and to a lesser extent at 5^o yaw. Streakline visualizations revealed a highly resolved periodic flow structure, coming from the inner leading edge of the wheel at these yaw angles. This observation, combined with helicity contours around the wheel lead us to suggest that vortex shedding from the inner rim along the leading edge of the wheel at these lower yaw angles is the likely explanation for this result. At higher yaw angles, the frequency analyses show a steady decline in the Strouhal No., going from St = 4.70 down to St = 3.36 at the 20^o yaw angle case. In examining the streakline visualizations, we see the evolution of a vortex structure forming in the upper quadrant on the outer edge of the wheel, and eventually extending to a point just ahead of the ground contact at the bottom of the wheel. We speculate that this larger structure becomes dominant going from lower angles of yaw to higher ones and as this structure grows, the rate of shedding slows down. In some instances, it was difficult to resolve power spectral density distributions. Future studies should be conducted at a higher temporal resolution to determine whether the Strouhal number results reported here would be affected.

An objective of this work was to establish a working CFD methodology to study the performance of an isolated, rotating bicycle wheel of commercial design, in contact with the ground. Good agreement with experimental wind tunnel studies suggests that the approach we outline holds considerable promise. Owing to the flexibility of this methodology, it is now possible to use CFD to provide more definitive answers on some of the open questions within the competitive cycling and triathlon communities. Issues such as the optimum wheel rim depth and cross-sectional profile, spoke count and shape, wheel diameter (650cc or 700cc) and tire size would benefit significantly from an independent critical analysis. Finally, we feel that inclusion and optimization of the front fork and frame and brake calipers in conjunction with a specific wheel is a straightforward extension of this work, and that such optimization studies would lead to significant performance improvements.

Acknowledgments

The authors would like to express their thanks to David Greenfield, President of Elite Bicycles, Inc., for his time spent discussing the current trends and technologies used in the design and production of present day bicycle racing wheels, forks and frames.

References

[1] Garcia-Lopez, J., Rodriguez-Marroyo, J.A., Juneau, C.-E., Peleteiro, J., Martinez, A.C. and Villa, J.G., 2008, "Reference values and improvements of aerodynamic drag in professional cyclists", J. Sports Sci., 26(3), pp. 277-286.
[2] Kyle, C.R, "Selecting Cycling Equipment", 2003. In High Tech Cycling, 2nd Edition, Burke, E.R, ed. Human Kinetics, pp. 1-48.
[3] Lukes, R.A., Chin, S.B. and Haake, S.J., "The Understanding and development of Cycling Aerodynamics", 2005, Sports Engineering, 8, pp. 59-74.
[4] Greenwell, D.I., Wood, N.J., Bridge, E.K.L and Add, R.J. 1995, "Aerodynamic characteristics of low-drag bicycle wheels", Aeronautical J., 99 (983), pp. 109-120.
[5] Zdravkovich, M.M., 1992, "Aerodynamics of bicycle wheel and frame", J. Wind Engg and Indust. Aerodynamics, 40, pp. 55-70.
[6] Sargent, L.R., "Carbon Bodied Bicycle Rim", U.S. Patent 5,975,645, Nov, 2, 1999.
[7] Hed, S.A and Haug, R.B., Bicycle Rim and Wheel", U.S. Patent 5,061,013, Oct. 29, 1991.
[8] Tew, G.S. and Sayers, A.T., 1999, "Aerodynamics of yawed racing cycle wheels", J. Wind Eng. Industr. Aerodynamics, 82, pp. 209-222.
[9] Kyle, C.R. and Burke, E. 1984, "Improving the racing bicycle", Mech. Eng., 106, pp. 34-35.
[10] Kyle, C.R., 1985, "Aerodynamic wheels", Bicycling, pp. 121-124.
[11] Kyle, C.R., 1991, "New aero wheel tests", Cycling Sci. pp. 27-32.
[12] Fackrell, J.E. and Harvey, J.K., 1973, "The Flowfield and Pressure Distribution of an Isolated Road Wheel", Advances on Road Vehicle Aerodynamics", Stephens, H.S., ed., BHRA Fluid Engineering, pp. 155-165.
[13] Fackrell, J.E., 1974, "The Aerodynamics of an Isolated Wheel Rotating in Contact with the Ground", Ph.D. Thesis, University of London, London, U.K.
[14] Fackrell, J.E. and Harvey, J.K., 1975, "The Aerodynamics of an Isolated Road Wheel", in Pershing, B. ed., Proc. of 2nd AIAA Symposium of Aerodynamics of Sports and Competition Automobiles, LA, Calif., USA, pp. 119-125.
[15] Wray, J, 2003, " A CFD Analysis into the effect of Yaw Angle on the Flow around an Isolated Rotating Wheel", Ph.D. Thesis, Cranfield University, U.K.
[16] McManus, J. and Zhang, X., 2006, "A Computational Study of the Flow Around an Isolated Wheel in Contact with the Ground", J. Fluids Engineering, 128, pp. 520-530.
[17] Spalart, P.R. and Allmaras, S.R., 1992, "A one-equation Turbulence Model for Aerodynamic Flows", 30th AIAA Aerospace Sciences Annual Meeting, Reno NV, USA, 6-9 January, AIAA Paper No. 92-0439.
[18] Shih, T.H., Liou, W.W., Shabbir, A., Yang, Z. and Zhu, J., 1995, "A New κ–ε Eddy Viscosity Model for High Reynolds Number Turbulent Flows", Comput. Fluids, 24(30), pp. 227-238.
[19] GAMBIT, Grid Generation Software Package, Version 2.4.6, ANSYS Inc., Pittsburgh, PA, 2008.
[20] AcuSolve, General Purpose CFD Software Package, Release 1.7e, ACUSIM Software, Mountain View, CA, 2008.
[21] Hughes, T.J.R., Franca, L.P. and Hulbert, G.M., 1989, "A new finite element formulation for computational fluid dynamics. VIII. The Galerkin/least-squares method for advective-diffusive equations", Comp. Meth. Appl. Mech. Engg., 73, pp 173-189.
[22] Shakib, F., Hughes, T.J.R. and Johan, Z., 1991, "A new finite element formulation for computational fluid dynamics. X. The compressible Euler and Navier-Stokes equations", Comp. Meth. Appl. Mech. Engg., 89, pp 141-219.
[23] Johnson, K and Bittorf, K., "Validating the Galerkin Least Square Finite Element Methods in Predicting Mixing Flows in Stirred Tank Reactors", Proceedings of CFD 2002, The 10th Annual Conference of the CFD Society of Canada, 2002.
[24] Jansen, K. E. , Whiting, C. H. and Hulbert, G. M., 2000, "A generalized-alpha method for integrating the filtered Navier-Stokes equations with a stabilized finite element method", Comp. Meth. Appl. Mech. Engg.", 190, pp 305-319.
[25] Spalart, P., Deck, S., Shur, M., Squires, K., Strelets, M. and Travin, A., 2006 "A New Version of Detached-Eddy Simulation, Resistant to Ambiguous Grid Densities", J. Theoretical and Computational Fluid Dynamics", 20, 181-195.
[26] FieldView, CFD Postprocessing Software Package, Version 12.01, Intelligent Light, Rutherford, NJ, 2007.
[27] Kuhnen, R., 2005, "Aerodynamische Laufrader: Gegen den Wind", TOUR Magazine, 9, pp. 24-31.
[28] Magnus, G., 1853, Uber die abweichung der gesechesse. Pogendorf's Ann. der Phys. Chem., 88, pp. 1–14
[29] Glauert, M.B., 1957, "The Flow past a Rapidly Rotating Circular Cylinder", Proc. Roy.Soc. Lond. A, 242, pp 108-115.
[30] Chew, Y.T., Cheng, M. and Luo, S.C., 1995, "A Numerical Study of Flow Past a Rotating Circular Cylinder using a Hybrid Vortex Scheme", J. Fluid Mech., 299, pp 35-71.
[31] Labraga, L., Kahissim, G., Keirsbuick, L and Beaubert, F., 2007, "An Experimental Investigation of the Separation Points on a Circular Rotating Cylinder in Cross Flow", 129, pp 1203-1211.